# Energy-loss spectroscopy of $C_{60}$ fullerenes with twisted electrons: Influence of orbital-angular-momentum transfer on plasmon generation

Michael Schüler and Jamal Berakdar
*Institut für Physik, Martin-Luther-Universität Halle-Wittenberg, Karl-Freiherr-von-Fritsch-Straße 3, 06120 Halle, Germany*
(Received 28 October 2016; published 30 November 2016)

Recent experimental progress in creating and controlling singular electron beams that carry orbital angular momentum allows for new types of local spectroscopies. We investigate theoretically the twisted-electron-energy-loss spectroscopy (EELS) from the $C_{60}$ fullerene. Of particular interest are the strong multipolar collective excitations and their selective response to the orbital angular momentum of the impinging electron beam. Based on *ab initio* calculations for the collective response, we compute EELS signals with twisted-electron beams, particularly in a transmission electron microscopy setup, and uncover the interplay between the plasmon polarity and the amount of angular momentum transfer.

DOI: 10.1103/PhysRevA.94.052710

## I. INTRODUCTION

Collective excitations in nanostructures are at the heart of the research field of nanoplasmonics [1]. A standard and widely utilized method to access the details of such collective modes is electron-energy-loss spectroscopy (EELS) [2]. With the advent of vortex or twisted beams [3–5], it is timely to explore the add-on features when performing EELS with such beams. A particular aspect of vortex beams is that they carry a definite and controllable amount of orbital angular momentum (OAM), which is related to the topological charge of the vortex. Remarkably, vortex beams were also realized in a transmission electron microscope (TEM), allowing thus for atomic spatial resolution. Typical phenomena associated with the OAM of the twisted beam are dichroism in magnetic systems [6] and different types of Landau states [7,8].

Using a concept similar to that for the generation of the vortex beams [9], the angular momentum after scattering from the probe can be determined. Exploiting this feature, one may employ vortex-based EELS to investigate the system response not only at a particular linear momentum transfer, but also for a well-defined orbital angular momentum transfer (OAMT). One consequence, for instance, is that multipolar excitations can be accessed even at small (linear) momentum transfer, which is known as the optical limit in conventional EELS.

A prominent molecular example, where the excitation energy varies significantly with the multipolarity, is the $C_{60}$ fullerene [10–12]. In our previous studies [13] we developed an accurate model, based on first-principle calculations, that is very suitable for studying EELS. In this paper we employ a slightly improved version of the model with the main focus on elucidating how the control of the OAMT can be utilized to map out multipolar excitations. After introducing the general theoretical formulation, we consider both the case of an isolated molecule and the case of a two-dimensional film of molecules. We show that by fixing the OAMT the encoded phase information results in specific features in the spectra. This effect is most pronounced for the spectroscopy of a single molecule, but it also prevails for crystallized $C_{60}$. Although we focus on the $C_{60}$ fullerene here, the methodology and the formula below are general and applicable to other systems.

The paper is organized as follows. In Sec. II we revisit the basic formulation of EELS in view of a more general projectile wave functions, such as "twisted" electrons. Our parametrization of the underlying plasmonic response of the system is also discussed. Based on this model, we first illustrate the control of the multipolarity in Sec. III by studying the vortex-based EELS from a single molecule. After that we turn to a crystallized surface. Atomic units are used unless stated otherwise.

## II. THEORETICAL FORMULATION

Given that the initial and final asymptotic states of the electrons are known and are denoted by, respectively, $\psi_i(\mathbf{r})$ and $\psi_f(\mathbf{r})$, Fermi's golden rule allows for the calculation of the transfer rate as [14]

$$\Gamma \propto \sum_{\alpha\neq 0} |\langle \Psi_\alpha, \psi_f | \hat{V}_{ee} | \Psi_0, \psi_i \rangle|^2 \delta(E_0 + \varepsilon_i - E_\alpha - \varepsilon_f), \quad (1)$$

where $|\Psi_0\rangle$ ($|\Psi_\alpha\rangle$) is the ground (excited) state of the target with corresponding energy $E_0$ ($E_\alpha$), $\varepsilon_{i,f}$ is the energy of the incoming or outgoing electrons, respectively, and $\hat{V}_{ee}$ is the Coulomb interaction. In a typical EELS setup the energy of the impinging electrons is much higher than the typical target excitations, which allows us to neglect exchange effects and simplify the transfer rate (1) to

$$\Gamma \propto \sum_{\alpha\neq 0} |\langle \Psi_\alpha | \hat{V}_{if} | \Psi_0 \rangle|^2 \delta(E_0 + \varepsilon_i - E_\alpha - \varepsilon_f). \quad (2)$$

The operator $\hat{V}_{if} = \int d\mathbf{r}\, V_{if}(\mathbf{r}) \hat{\psi}^\dagger(\mathbf{r}) \hat{\psi}(\mathbf{r})$ (expressed in second quantization) stands for the effective potential acting on the target,

$$V_{if}(\mathbf{r}) = \int d\mathbf{r}' v(\mathbf{r}-\mathbf{r}') \psi_i^*(\mathbf{r}') \psi_f(\mathbf{r}'), \quad (3)$$

while $v(\mathbf{r}) = 1/|\mathbf{r}|$ is the Coulomb potential. The fluctuation-dissipation theorem [15] provides a link of the expression (2) to the density-density response function [16] $\chi(\mathbf{r},\mathbf{r}';\omega)$ by

$$\Gamma(\omega) \propto -\int d\mathbf{r} \int d\mathbf{r}' V_{if}(\mathbf{r}) \mathrm{Im}[\chi(\mathbf{r},\mathbf{r}';\omega)] V_{if}^*(\mathbf{r}'). \quad (4)$$

Here $\omega = \varepsilon_i - \varepsilon_f > 0$ defines the energy loss. Alternatively, one can combine the convolution with the Coulomb potential in Eq. (3) with the response function by introducing the dynamically screened interaction $W(\mathbf{r},\mathbf{r}';\omega)$

 

$= v(\mathbf{r}-\mathbf{r}') + \delta W(\mathbf{r},\mathbf{r}';\omega)$ with

$$\delta W(\mathbf{r},\mathbf{r}';\omega) = \int d\mathbf{r}_1 \int d\mathbf{r}_2 v(\mathbf{r}-\mathbf{r}_1)\chi(\mathbf{r}_1,\mathbf{r}_2;\omega)v(\mathbf{r}_2-\mathbf{r}'), \tag{5}$$

yielding

$$\Gamma(\omega) \propto -\int d\mathbf{r} \int d\mathbf{r}' \psi_i^*(\mathbf{r})\psi_f(\mathbf{r}) \times \mathrm{Im}[\delta W(\mathbf{r},\mathbf{r}';\omega)]\psi_i(\mathbf{r}')\psi_f^*(\mathbf{r}'). \tag{6}$$

We note that Eq. (6) can also be derived from classical considerations [17].

So far the wave function of the ingoing or outgoing electrons have not been specified. Depending on the actual experimental setup, a wide range of scenarios is possible. Here we focus on spectroscopy with beams carrying the orbital angular momentum, called twisted electron beams. They can be described by [18]

$$\varphi_{\ell k}(\mathbf{r}) = e^{i\ell\phi}e^{ikz}F_\ell(R), \tag{7}$$

where cylindrical coordinates $(R,\phi,z)$ have been used. For later convenience, we express the position vectors as $\mathbf{r} = \mathbf{R} + z\mathbf{e}_z$, with $|\mathbf{R}| = R$, and $\mathbf{e}_z$ stands for the unit vector in the $z$ direction. Note that the radial profile $F_\ell(R)$ (which is kept general at this point) can depend on a transverse momentum component. In the case of wide beams as compared to the typical system size, transverse momentum transfer, however, does not play an important role [19]. We will hence omit this momentum dependence of the profiles $F_\ell(R)$. The normalization is fixed by the orthonormality condition

$$\langle\varphi_{\ell k}|\varphi_{\ell' k'}\rangle = \delta_{\ell\ell'}\delta(k-k'). \tag{8}$$

Provided such twisted electrons scatter from a target besides the momentum in the longitudinal direction, *angular* momentum might be transferred. The consequences of this effect depend on how the outgoing electrons are detected. We now focus on two typical scenarios.

### A. Conventional TEM

In the TEM setup electrons are collected in a wide-angle analyzer after being transmitted through the sample [17,20]. For this reason, the angular momentum of the outgoing electrons is not determined. Assuming the electron beam is prepared in a twisted state $\varphi_{\ell k}(\mathbf{r})$ and is detected with transverse momentum $\mathbf{p}_\perp$, one finds for the momentum-resolved EELS signal

$$\frac{d\Gamma_\ell(\omega)}{d\mathbf{p}_\perp} \propto -\int d\mathbf{r} \int d\mathbf{r}' e^{i\ell(\phi'-\phi)}e^{i\mathbf{p}_\perp\cdot(\mathbf{R}-\mathbf{R}')}e^{i\omega(z'-z)/k} \times F_\ell^*(R)F_\ell(R')\mathrm{Im}[\delta W(\mathbf{r},\mathbf{r}';\omega)]. \tag{9}$$

Here we have approximated the longitudinal momentum transfer $q$ by $q = \omega/k$, which is obtained by a first-order Taylor expansion in $\omega/\varepsilon_i$. The angular momentum of the twisted beam thus directly influences the EELS signal provided the angular distribution is recorded. Integrating over all possible detection directions, on the other hand,

$$\Gamma_\ell(\omega) = \int d\mathbf{p}_\perp \frac{d\Gamma(\omega)}{d\mathbf{p}_\perp},$$

yields the total cross section [17]

$$\Gamma_\ell(\omega) \propto -\int d\mathbf{R} \int_{-\infty}^{\infty} dz \int_{-\infty}^{\infty} dz' e^{i\omega(z'-z)/k}|F_\ell(R)|^2 \times \mathrm{Im}[\delta W(\mathbf{R}+z\mathbf{e}_z,\mathbf{R}+z'\mathbf{e}_z;\omega)]. \tag{10}$$

An important conclusion to be drawn from Eq. (10) is that the influence of the angular momentum on the EELS spectra enters through the radial beam profile (which depends on $\ell$). This is the case if the signal is collected by integrating over all possible directions.

### B. Detection of angular momentum

The situation changes if the angular momentum of the scattered electrons is detected explicitly. Experimentally, this can be achieved by a holographic vortex filter that the scattered beam traverses, thus separating the different angular momentum components by the propagation direction [21]. In this case the OAMT $\Delta\ell = \ell - \ell'$ becomes an important control parameter [6]. Note that this characterization is only possible if the respective axes of the ingoing and outgoing beams coincide. In general, this is an approximation that is adequate for targets smaller than the beam waist [19]. Based on this assumption, we can most conveniently compute the effective potentials by solving Poisson's equation

$$\nabla^2 V_{if}(\mathbf{r}) = -4\pi\varphi_{\ell k}^*(\mathbf{r})\varphi_{\ell' k'}(\mathbf{r}), \tag{11}$$

exploiting the cylindrical symmetry. The ansatz $V_{if}(\mathbf{r}) = e^{i\Delta\ell\phi}e^{iqz}w_{\ell,\ell'}(q;R)$ (where $q = k - k'$) reduces Eq. (11) to the radial Poisson equation

$$\left[\frac{d^2}{dR^2} + \frac{1}{R}\frac{d}{dR} + \frac{\Delta\ell^2}{R^2} - q^2\right]w_{\ell,\ell'}(q;R) = -4\pi F_\ell(R)F_{\ell'}(R), \tag{12}$$

which is solved in terms of the its Green's function $g_{mq}(R,R') = \pi(2-\delta_{m,0})I_m(qR_<)K_m(qR_>)$. Here $I_m(x)$ and $K_m(x)$ denote the modified Bessel functions of the first and second kinds, respectively. As usual, $R_< = \min(R,R')$ and $R_> = \max(R,R')$. For the radial part of the potential one finds

$$w_{\ell,\ell'}(q;R) = -4\pi\int_0^\infty dR'R'g_{|\ell-\ell'|q}(R,R')F_\ell^*(R')F_{\ell'}(R'). \tag{13}$$

For a target possessing almost perfect spherical symmetry such as the $C_{60}$ molecule, the expansion of the density-density response function in terms of fluctuation densities reads

$$\chi(\mathbf{r},\mathbf{r}';\omega) = \sum_{\nu LM}\xi_{\nu L}(\omega)\rho_{\nu L}(r)\rho_{\nu L}(r')Y_{LM}^*(\hat{\mathbf{r}})Y_{LM}(\hat{\mathbf{r}}'). \tag{14}$$

Therefore, Eq. (4) attains the form

$$\Gamma_{\ell\ell'}(\omega) \propto -\sum_{\nu LM}\mathrm{Im}[\xi_{\nu L}(\omega)]\left|\int d\mathbf{r}\,\rho_{\nu L}(r)Y_{LM}^*(\hat{\mathbf{r}})V_{if}(\mathbf{r})\right|^2. \tag{15}$$

An important special case occurs if the beam axis points through the center of the $C_{60}$ molecule, as the integration over

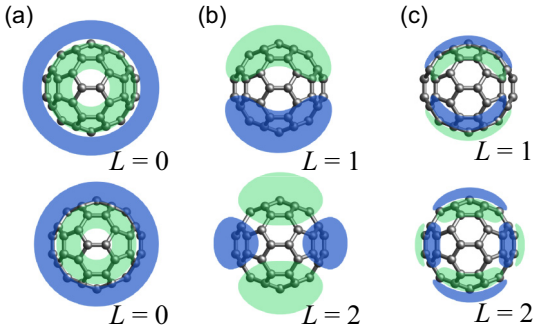


FIG. 1. Illustration of the plasmon modes by the area in the $x$-$z$ plane where the model fluctuation densities $\rho_{\nu L,M=0}(\mathbf{r}) > 0$ (light green) and $\rho_{\nu L,M=0}(\mathbf{r}) < 0$ (darker blue). (a) Volume plasmons $V1$ (top) and $V2$ (bottom), (b) symmetric surface plasmons for $L = 1,2$, and (c) antisymmetric surface modes with $L = 1,2$.

the angle $\phi$ is simplified by

$$\int_0^{2\pi} d\phi\, Y_{LM}^*(\hat{\mathbf{r}}) e^{i\Delta\ell\phi} = 2\pi\, \widetilde{P}_L^M(\cos\theta)\delta_{\Delta\ell,M}. \quad (16)$$

Here $\widetilde{P}_L^M(x)$ stands for the associated Legendre polynomials normalized in accordance with the spherical harmonics. The selection rule $\Delta\ell = M$ limits the sum over $L$ by $L \geqslant |\Delta\ell|$ in Eq. (15) and hence excludes certain multipolar modes.

### C. Density-density response of the $C_{60}$ molecule

The central ingredient determining the (vortex) EELS signal is the density-density response function of the system, which comprises all types of excitations present in the system. This includes plasmons and particle-hole ($p$-$h$) excitations. Qualitative insights into the collective density fluctuations can be gained from semiclassical considerations [22,23], where the electronic density $C_{60}$ molecule is approximated by a spherical shell. The density can thus only fluctuate at the inner and the outer surface, respectively, giving rise to symmetric or antisymmetric oscillations and a volume plasmon. Our parametrization from Ref. [13] provides an accurate fit to the full-fledged first-principles calculations based on time-dependent density-functional theory (TDDFT) and yet allows for an intuitive classification of the plasmon modes as given in the semiclassical model. In particular, the density-density response function $\chi(\mathbf{r},\mathbf{r}';\omega)$ is expanded as in Eq. (14), identifying the index $\nu$ with the radial quantum numbers. We distinguish between symmetric surface (SS) plasmons characterized by $\nu$ equal to the SS and multipolarity $L \geqslant 1$, antisymmetric surface (AS) plasmons (with $\nu$ equal to the AS and $L \geqslant 1$), and two types of volume plasmons ($\nu = V1, V2$ and $L = 0$). The quenching of the volume plasmons (which is lacking in the semiclassical shell model) is a consequence of the delocalized nature of the electron density. The plasmon modes entering our model are sketched (up to $L = 2$) in Fig. 1.

The model from Ref. [13] is constructed from fitting functions for the spectra $\xi_{\nu L}(\omega)$ and the fluctuation densities $\rho_{\nu L}(r)$, which allows for an accurate modeling of the full density-density response function [24]. Here we use an improved version of the fitting procedure for the frequency dependence. Taking the spectral functions $\xi_{\nu L}^{\mathrm{TDDFT}}(\omega)$ from our

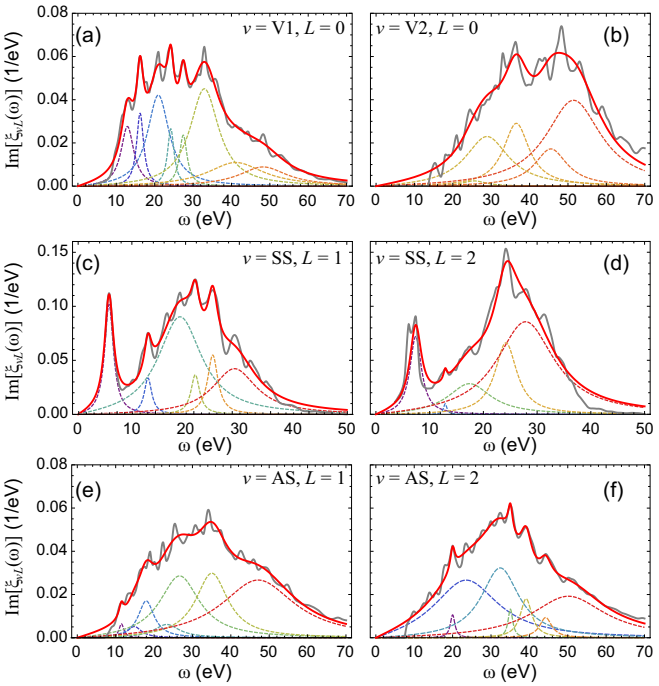


FIG. 2. Multipeak fits of the frequency dependence $\xi_{\nu L}(\omega)$ of the density-density response function [cf. Eq. (14)] in terms of (a) and (b) the volume, (c) and (d) the symmetric surface, and (e) and (f) the antisymmetric surface plasmons. Solid gray lines show the TDDFT results $\xi_{\nu L}^{\mathrm{TDDFT}}(\omega)$ from Ref. [13]; solid red lines the fitted frequency dependence $\xi_{\nu L}^{\mathrm{fit}}(\omega)$ and dashed lines the individual peak contributions [see Eq. (17)].

TDDFT calculations, we select the dominant peaks assuming a generic form

$$\xi_{\nu L}^{\mathrm{TDDFT}}(\omega) \approx \xi_{\nu L}^{\mathrm{fit}}(\omega) = \sum_{i=1}^{N_{\nu L}} A_{i\nu L} \frac{2\Omega_{i\nu L}}{(\omega + i\Gamma_{i\nu L})^2 - \Omega_{i\nu L}^2}. \quad (17)$$

The weights $A_{i\nu L}$, peak frequencies $\Omega_{i\nu L}$, and broadening $\Gamma_{i\nu L}$ are then obtained from a least-squares fit. The obtained spectra (up to $\ell = 2$) are compared to the results of the *ab initio* calculations from Ref. [13] in Fig. 2.

## III. RESULTS

With the general theoretical formulation from Sec. II and an accurate model for the fluctuation densities and the corresponding spectra at hand, we can now analyze the inelastic scattering of the vortex beams from the $C_{60}$ molecule. In line with a typical experimental realization [4,7,25], we choose Laguerre-Gauss modes as an approximation to the profile $F_\ell(R)$ of the vortex beams:

$$F_\ell(R) = \frac{2}{\sqrt{\ell!}W_0}\left(\frac{\sqrt{2}R}{W_0}\right)^{|\ell|} e^{-(R/W_0)^2} L_{|\ell|}^p(2(R/W_0)^2). \quad (18)$$

Here $L_{|\ell|}^p(x)$ denote the associated Laguerre polynomials. We set the radial node number to be $p = 0$. Note that $\varphi_\ell(\mathbf{r})$ is not an eigenstate of the free-particle Hamiltonian in this case. However, as the energy is carried in the longitudinal ($z$) direction, the energy of the beam is still sharply defined.

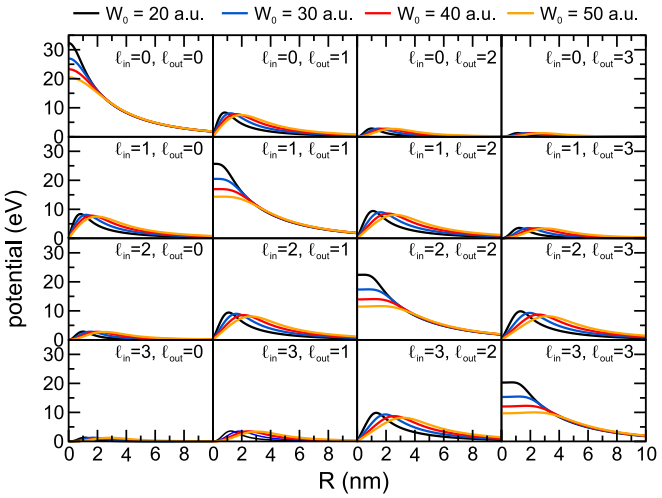


FIG. 3. Radial part $w_{\ell_{\rm in},\ell_{\rm out}}(q;R)$ of the effective potential for the typical value $q = 0.01$ a.u., with $0 \leqslant \ell_{\rm in} \leqslant 3$ and $0 \leqslant \ell_{\rm out} \leqslant 3$.

Representing the vortex beams by the Laguerre-Gauss profile (18) shifts the dependence on the transverse momentum to the beam waist $W_0$. We assume that $W_0$ is preserved upon scattering, an approximation that relies on the small size of the molecules on the scale of $W_0$. By varying $W_0$ of the outgoing beam, we confirm that this assumption is justified to very good accuracy. This can be understood by the weak dependence of the effective potential on the beam profile, which is discussed now.

### A. Effective potential

In Fig. 3 we present the radial part of the effective potential $V_{if}(\mathbf{r})$ as discussed in Sec. II B for typical values of the beam waist $W_0$. As we can infer from Fig. 3, the effective potential quickly drops with increasing OAMT $\Delta\ell = \ell_{\rm in} - \ell_{\rm out}$, which is explained by the decreasing overlap of the respective beam profiles. The potential displays a plateau behavior around $R = 0$ for $\ell_{\rm in} = \ell_{\rm out}$, while it vanishes at this point for $\ell_{\rm in} \neq \ell_{\rm out}$. The asymptotic behavior is determined by $e^{-qR}/\sqrt{qR}$, i.e., for small momentum transfer as typically encountered in high-energy EELS, the effective potential can be quite long ranged, affecting the molecules situated far away from the beam axis. This is very different from photons carrying orbital angular momentum. In a conventional EELS setup, the effective potential reads $4\pi/q^2 e^{i\mathbf{q}\cdot\mathbf{r}}$ and thus exhibits a quadratic divergence for $q \to 0$. The effective potential caused by scattering of twisted electrons, on the other hand, shows a logarithmic divergence, as expected for a two-dimensional regularization due to using beams with a finite width.

### B. Loss spectra: Beam focused on a molecule

If the beam axis passes through the molecule's center the selectivity with respect to the OAMT is most pronounced due to Eq. (16). As the energy of impinging electrons is high ($\varepsilon_i =$ 60 keV), the longitudinal momentum transfer is in the range of $q \simeq \omega/\sqrt{2\varepsilon_i} \lesssim 0.03$ a.u. approaching the optical limit for the $C_{60}$ molecule. As previously discussed [13], the dominant excitations for small $q$ are the SS plasmons and the dipole SS plasmon in particular. Volume plasmons, however, can also be induced due to the radial dependence of the beam. Increasing the OAMT $|\Delta\ell|$, we expect that the loss spectra are shifted to higher energies, as the frequencies of the SS plasmons grow with the multipolarity.

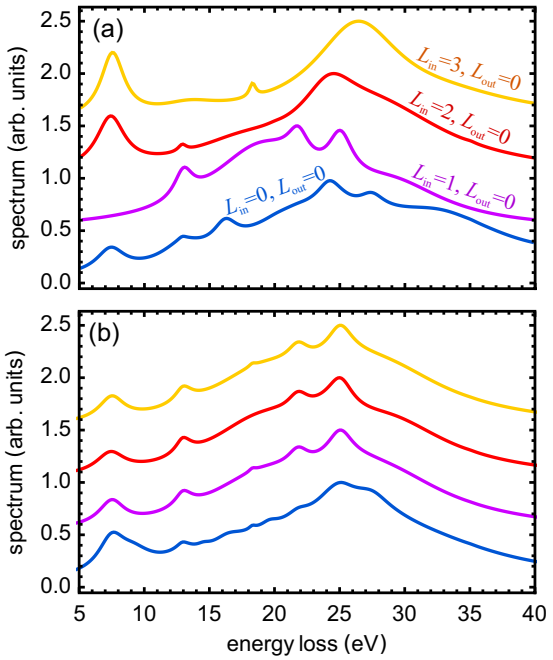


FIG. 4. Twisted-electron-energy-loss spectra when the beam axis coincides with the center of the $C_{60}$ molecule (beam waist $W_0 =$ 30 a.u.). (a) Fixed outgoing angular momentum $L_{\rm out} = 0$ for different angular momenta $L_{\rm in}$ of the impinging beam. (b) Loss spectra for the same incoming angular momenta as in (a), but without fixing $L_{\rm out}$. The spectra have been normalized and shifted for better visibility.

To confirm this dependence, we computed the loss spectra for different values of $\ell_{\rm in}$ and fixed the angular momentum of the scattered electrons at $\ell_{\rm out} = 0$. The OAMT to the system is thus $\Delta\ell = \ell_{\rm in}$.

To evaluate Eq. (15) we use the radial fluctuation densities $\rho_{\nu L}(r)$ and plasmon spectra $\xi_{\nu L}(\omega)$ from Ref. [13]. After solving the radial Poisson equation (12) by Eq. (13), the effective potential $V_{if}(\mathbf{r})$ is projected on the spherical harmonics with respect to the molecule's center. Finally, the remaining integration over the distant from the center $r$ is performed. The momentum transfer is replaced by $q = \omega/k$.

The resulting normalized spectra are presented in Fig. 4(a). For $\ell_{\rm in} = \ell_{\rm out} = 0$, only volume plasmons can be excited, leading to a broad loss spectrum, which is consistent with the frequency dependence in Fig. 2(a). For $\Delta\ell = 1$, dipole plasmons can be induced (predominantly the SS plasmon). The loss spectrum is therefore similar to the optical absorption spectrum [26]. Increasing the OAMT, the plasmon dispersion with respect to the multipolarity leads to a shift of the spectra to higher energies. Furthermore, due to the changed beam profile, AS plasmons can also be induced, which further shifts the spectra. The dependence of the loss spectra on the angular momenta is quantified in Table I, where we give the overall peak positions (obtained by a Lorentzian fit) as a function of $\ell_{\rm in}$ and $\ell_{\rm out}$.

TABLE I. Energy losses $\omega$ where the cross section is peaked, computed by performing a fit by a single Lorentzian in the peak region. The beam has a waist of $W_0 = 30$ a.u. and is aligned with the molecule's center. Values are shown in eV.

| $\ell_{out}$ \ $\ell_{in}$ | 0 | 1 | 2 | 3 | 4 |
|---|---|---|---|---|---|
| 0 | 26.29 | 21.88 | 25.55 | 26.81 | 27.0 |
| 1 | 21.88 | 24.97 | 21.87 | 25.53 | 26.7 |
| 2 | 25.55 | 21.87 | 24.89 | 21.87 | 25.5 |
| 3 | 26.81 | 25.53 | 21.87 | 24.85 | 21.8 |
| 4 | 27.07 | 26.74 | 25.53 | 21.87 | 24.82 |

The situation changes drastically if the requirement of detecting the outgoing angular momentum is dropped. As elaborated upon in Sec. II A, the effect of the OAMT should diminish. This is indeed consistent with our results for this case [Fig. 4(b)]. The loss spectra exhibit a very weak dependence on the initial angular momentum of the beam, which arises due to a changed beam profile only. Hence, not detecting the angular momentum leads to a loss of phase information that is directly reflected in the featureless spectra.

### C. Loss spectra: Crystalline phase

Conducting an EELS experiment on isolated $C_{60}$ is very challenging, as preparing single molecules on the substrate used in the TEM setup is hardly possible. It is much more likely that the fullerenes crystallize on the surface of the substrate, forming a few layers of an fcc crystal [lattice constant $a(C_{60}) = 1.4154$ nm at room temperature]. To describe this setup theoretically, based on the previously employed model, we assume that the individual contributions of the molecules can be summed to obtain an adequate approximation to the response of the crystal:

$$\Gamma^{\mathrm{crys}}_{\ell\ell'}(\omega) \propto -\sum_{n\in\mathrm{latt}}\sum_{\nu LM}\mathrm{Im}[\xi_{\nu L}(\omega)] \times\left|\int d\mathbf{r}\,\rho_{\nu L}(r)Y^*_{LM}(\hat{\mathbf{r}})V_{if}(\mathbf{r}+\mathbf{r}_n)\right|^2. \quad (19)$$

Here $\mathbf{r}_n$ denotes the lattice sites. This treatment ignores the hybridization of the plasmon modes into corresponding bands. The significance of such effects is not completely understood at the moment; calculations for the condensed phase [27] report quite similar spectra as compared to the gas phase [23]. As thin films are best suited for TEM experiments, we consider a single layer of molecules here. The geometry of the $C_{60}$ is compared to the typical beam extensions in Fig. 5.

Note that the beam axis does not pass through most of the molecules' centers, resulting in less sharply defined OAMT (which is defined with respect to the beam). The scenario of decentered beams questions the assumption of keeping the beam axis and waist $W_0$ constant throughout the scattering process. For the molecules located not to far from the vortex center, including the area of maximum intensity (which has the largest contribution to the total signal), the validity of this approximation has been underpinned in Ref. [28].

Analogously to the single-molecule case, we first analyze the scenario where the angular momentum of the outgoing

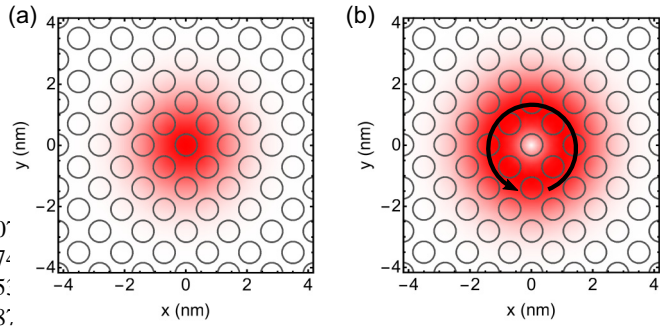


FIG. 5. Illustration of the (111) surface layer of $C_{60}$ molecules (gray circles) along with the beam profile $F_\ell(R)$ (density plot) for (a) $\ell = 0$ and (b) $\ell = 1$. The direction of the phase variation is indicated by the black arrow.

electrons is explicitly detected. Evaluating the cross section (19) yields the loss spectra presented in Fig. 6. First we note that the difference between the spectra, when varying the OAMT, is not as pronounced as for the single molecules. This is a result of the collective response of many molecules located off-center with respect to the beam axis, as the OAM (which depends on the reference coordinate system) of the beam is blurred when considered from the fullerenes' point of view. Hence, despite the total OAMT being fixed, off-center molecules experience different many OAM components. Hence, the multipolar excitations cannot be controlled as efficiently as before. Nevertheless, the phase information

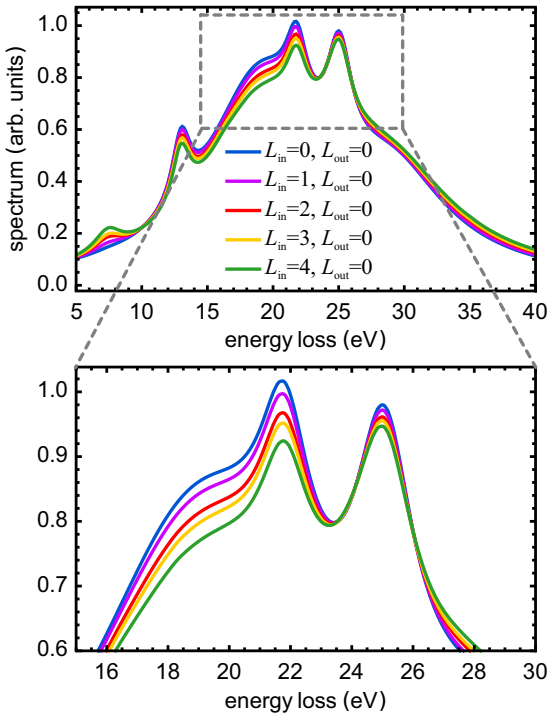


FIG. 6. Loss spectra for scattering from one layer of fcc $C_{60}$ ($W_0 = 30$ a.u.) for different values of the OAM of the ingoing beam $L_{in}$ and fixed outgoing OAM $L_{out} = 0$ (geometry as in Fig. 5). The curves have been normalized to the same frequency-integrated value. The region in the dashed rectangle is magnified in the bottom panel.

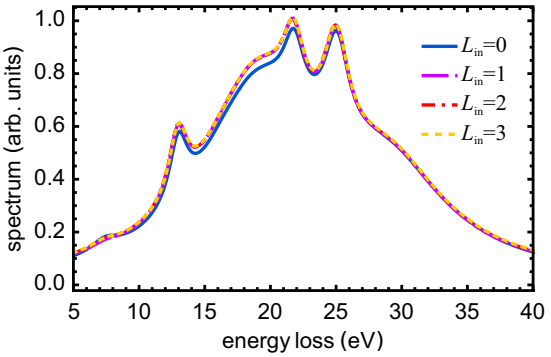


FIG. 7. Loss spectra for scattering from one layer of fcc $C_{60}$ as in Fig. 6, but without fixing the outgoing OAM $L_{out}$.

encoded in the OAM of the vortex beam leads to notable differences in the loss spectra. Generally, the trend is as in Sec. III B: The increased probability to induce multipolar excitations with growing OAMT shifts the spectra to higher frequencies. This behavior is mostly reflected in the less and less pronounced shoulder at $\omega \simeq 19$ eV (see the zoom in the bottom panel in Fig. 6), which corresponds to the dominant feature of the SS dipole plasmon [see Fig. 2(c)]. Hence, the contribution of the dipolar plasmons is suppressed. Interestingly, the peak $\omega \simeq 7.5$ eV is enhanced with increasing OAMT as well. This peak corresponds to series of particle-hole excitations $p$-$h$ in the bound-state manifold [29]. The increasing weight of $p$-$h$ excitations as compared to the plasmons is a signature of a more inhomogeneous driving acting on the system, as collective excitations only exist at small wave vectors (small angular momenta, respectively). This effect can also be observed in Fig. 4. Mapping out the $p$-$h$ excitations induced by vortex beams based on our *ab initio* approach from Ref. [29] is left for future work.

To demonstrate that the modification of the spectra in Fig. 6 depends on the phase of the vortex beam, we recompute the loss spectra assuming that the OAM of the outgoing electrons is not detected (Fig. 7). Analogously to the discussion in Sec. III B, we find that the spectra for different ingoing OAM $L_{in}$ are basically identical, except for the case $L_{in} = 0$. The latter is due to a quite different beam profile [see Fig. 5(a)]. Hence, it is truly the OAM of the vortex beams (which is pure phase effect) that can induce multipolar excitations and thus give rise to specific features in the loss spectra.

## IV. CONCLUSION

We presented the theoretical description of twisted-electron-energy-loss spectra for cases when (i) the scattered electrons are detected in the full solid angle and (ii) the angular momentum of the scattered electrons is detected. While for (i) the angular momentum of the beam, encoded in the phase, has no influence, we showed that it plays an important role in case (ii), particularly if the beam is aligned with the single-molecule center. We applied the developed theory for EELS with twisted electrons for fixed molecules and for a single layer of crystallized fullerenes. The numerical findings are in line with the formal expectations: Measuring the outgoing OAM of the beam allows controlling the OAMT and thus the multipolar excitations. This is directly reflected in the loss spectra. In contrast, detecting only the energy of the scattered electrons leads to almost identical spectra with varying OAM, since the phase information is lost and only the varying beam profile influences the overall spectra. So we advocate the OAM-resolved vortex-based EELS as a powerful technique to access new information about the system's excitations, particularly those of multipolar character.

## ACKNOWLEDGMENTS

We are indebted to Thomas Schachinger and Michael Stöger-Pollach for fruitful discussions and important insights from the experimental point of view, as well as to Yaroslav Pavlyukh for numerous discussions. Financial support through grants from the German Research Foundation, Grant No. SFB762, and the Priority Programme 1840 "Quantum Dynamics in Tailored Laser Fields" is gratefully acknowledged.

[1] S. A. Maier and H. A. Atwater, J. Appl. Phys. **98**, 011101 (2005).
[2] P. Schattschneider, *Fundamentals of Inelastic Electron Scattering* (Springer Science & Business Media, New York, 2012).
[3] J. Verbeeck, H. Tian, and P. Schattschneider, Nature (London) **467**, 301 (2010).
[4] R. Van Boxem, B. Partoens, and J. Verbeeck, Phys. Rev. A **91**, 032703 (2015).
[5] G. Guzzinati, A. Béché, H. Lourenço-Martins, J. Martin, M. Kociak, and J. Verbeeck, arXiv:1608.07449.
[6] S. Lloyd, M. Babiker, and J. Yuan, Phys. Rev. Lett. **108**, 074802 (2012).
[7] K. Y. Bliokh, P. Schattschneider, J. Verbeeck, and F. Nori, Phys. Rev. X **2**, 041011 (2012).
[8] P. Schattschneider, T. Schachinger, M. Stöger-Pollach, S. Löffler, A. Steiger-Thirsfeld, K. Y. Bliokh, and F. Nori, Nat. Commun. **5**, 4586 (2014).
[9] V. Grillo, G. C. Gazzadi, E. Mafakheri, S. Frabboni, E. Karimi, and R. W. Boyd, Phys. Rev. Lett. **114**, 034801 (2015).
[10] A. V. Verkhovtsev, A. V. Korol, A. V. Solov'yov, P. Bolognesi, A. Ruocco, and L. Avaldi, J. Phys. B **45**, 141002 (2012).
[11] A. V. Verkhovtsev, A. V. Korol, and A. V. Solov'yov, Phys. Rev. A **88**, 043201 (2013).
[12] C. Z. Li, Z. L. Mišković, F. O. Goodman, and Y. N. Wang, J. Appl. Phys. **113**, 184301 (2013).
[13] M. Schüler, J. Berakdar, and Y. Pavlyukh, Phys. Rev. A **92**, 021403 (2015).
[14] C. J. Joachain, *Quantum Collision Theory* (North-Holland, Amsterdam, 1975).
[15] G. Giuliani and G. Vignale, *Quantum Theory of the Electron Liquid* (Cambridge University Press, Cambridge, 2005).
[16] G. Onida, L. Reining, and A. Rubio, Rev. Mod. Phys. **74**, 601 (2002).
[17] F. J. García de Abajo, Rev. Mod. Phys. **82**, 209 (2010).

[18] J. Verbeeck, H. Tian, and A. Béché, Ultramicroscopy **113**, 83 (2012).
[19] P. Schattschneider, S. Löffler, and J. Verbeeck, Phys. Rev. Lett. **110**, 189501 (2013).
[20] R. F. Egerton, Rep. Prog. Phys. **72**, 016502 (2009).
[21] T. Schachinger, A. Steiger-Thirsfeld, S. Löffler, M. Stöger-Pollach, D. Pohl, B. Rellinghaus, and P. Schattschneider, *The 16th European Microscopy Congress* (Wiley, New York, 2016).
[22] A. Verkhovtsev, A. V. Korol, and A. V. Solov'yov, Eur. Phys. J. D **66**, 253 (2012).
[23] P. Bolognesi, L. Avaldi, A. Ruocco, A. Verkhovtsev, A. V. Korol, and A. V. Solov'yov, Eur. Phys. J. D **66**, 254 (2012).
[24] M. Schüler, Y. Pavlyukh, P. Bolognesi, L. Avaldi, and J. Berakdar, Sci. Rep. **6**, 24396 (2016).
[25] T. Schachinger, S. Löffler, M. Stöger-Pollach, and P. Schattschneider, Ultramicroscopy **158**, 17 (2015).
[26] A. Reinköster, S. Korica, G. Prümper, J. Viefhaus, K. Godehusen, O. Schwarzkopf, M. Mast, and U. Becker, J. Phys. B **37**, 2135 (2004).
[27] P. Koval, M. P. Ljungberg, D. Foerster, and D. Sánchez-Portal, Nucl. Instrum. Methods Phys. Res. Sect. B **354**, 216 (2015).
[28] P. Schattschneider, S. Löffler, M. Stöger-Pollach, and J. Verbeeck, Ultramicroscopy **136**, 81 (2014).
[29] S. Usenko, M. Schüler, A. Azima, M. Jakob, L. L. Lazzarino, Y. Pavlyukh, A. Przystawik, M. Drescher, T. Laarmann, and J. Berakdar, arXiv:1605.07858.